



**HORIZON 2020**

## **HORIZON 2020 RESEARCH AND INNOVATION FRAMEWORK PROGRAMME OF THE EUROPEAN ATOMIC ENERGY COMMUNITY**

### **Nuclear Fission and Radiation Protection 2018 (NFRP-2018-4)**

Project acronym: **SANDA**

Project full title: **Solving Challenges in Nuclear Data for the Safety of European Nuclear facilities**

Grant Agreement no.: **H2020 Grant Agreement number: 847552**

Workpackage N°: **WP1**

Identification N°: **D1.7**

Type of document: **Deliverable**

Title: Report on the development and performances of the new detectors for capture cross section measurements at n-TOF

Dissemination Level: **PU**

Reference:

Status: **VERSION 1**

Comments: ....

	Name	Partner	Date	Signature
Prepared by:	E. Mendoza et al.	1	07-09-2023	
WP leader:	M. Kerveno	5	07-09-2023	mkerveno
IP Co-ordinator:	E. González	1	07-09-2023	

## Executive summary

The second n\_TOF experimental area (EAR-2), built in 2015 and located at 20 m from the spallation target, is ~300 times more intense (30 times more neutrons and 10 times shorter flight path) than the 200 m long flight path of n\_TOF (EAR-1). Such a high neutron flux allows performing measurements at n\_TOF with more radioactive and/or lower mass samples. However, from the point of view of the capture detection systems, counting rates are two orders of magnitude larger than in EAR-1, and signal to background ratios are similar to those in EAR-1. For this reason, it is critical to have detectors capable of standing high reaction rates and better background rejection capabilities. This task is devoted to develop new detection systems for capture cross section measurements on actinides.

Two possibilities have been considered. The first possibility is a segmented Total Energy Detector (sTED), and the second is to adapt a new  $\gamma$ -ray detector with imaging capabilities (i-TED) to the capture cross section measurements of actinides in EAR-2.

Concerning the first detector development, the first idea was to use an array of inorganic scintillators, like Cs<sub>2</sub>LiYCl<sub>6</sub>:Ce (CLYC). However, after some investigations it was found that a much better performance would be obtained with small organic scintillators made of C<sub>6</sub>D<sub>6</sub>. We have designed, built, and tested extensively this new neutron capture detector (sTED). The results obtained have been very positive, showing that this detector is capable of measuring capture cross sections at the n\_TOF EAR2 up to energies of at least hundreds of keV. In fact, this new detector has already been used to carry out several neutron capture measurements at n\_TOF EAR2: <sup>79</sup>Se, <sup>94</sup>Nb, <sup>160</sup>Gd and <sup>94,95,96</sup>Mo. The results of the work related to the sTED are shown in Part I of this document.

Concerning the second detector development, measurements and analysis have been carried out with an i-TED module at n\_TOF EAR2 in order to characterize its response to very high-count rates and to explore weaknesses and possible technical solutions. The major technical limitation, of the actual i-TED system, is ascribed to the maximum count-rate capability of 500 kHz/detector, which is mainly constrained by the large number of readout channels (320 channels per module) and the ASIC-based readout front-end electronics required for such a large number of channels. Possible solutions to the aforementioned limitation will depend on the availability of new-generation ASIC electronics capable of coping with higher count-rates. The results of the work related to the i-TED are shown in Part II of this document.

PART I: A Segmented Total Energy Detector (sTED)  
optimized for (n, $\gamma$ ) cross-section measurements at n\_TOF  
EAR2

V. Alcayne<sup>a</sup> , D. Cano-Ott<sup>a</sup>, J. García<sup>a</sup> , E. González-Romero<sup>a</sup> , T.  
Martínez<sup>a</sup> , E. Mendoza<sup>a</sup> , A. Pérez de Rada<sup>a</sup> , J. Plaza<sup>a</sup> , A. Sánchez-  
Caballero<sup>a</sup>

<sup>a</sup>*Centro de Investigaciones Energéticas Medioambientales y Tecnológicas  
(CIEMAT), Spain.*

# 1 Introduction

The neutron time-of-flight facility n\_TOF, at CERN is focused on performing measurements of neutron-induced reaction cross-sections of interest to nuclear technologies, astrophysics, and other applications. The facility uses as a neutron source a massive lead spallation target coupled to the CERN-PS 20 GeV/c proton beam and is endowed with three experimental areas: Experimental Area 1 (EAR1) with  $\sim 8 \cdot 10^5$  protons per pulse, located at 185 m [1] horizontally from the spallation target, Experimental Area 2 (EAR2) with  $\sim 4 \cdot 10^7$  protons per pulse operational since 2014 and located vertically at 20 m from the spallation target [2], and the recent NEAR station with  $\sim 4 \cdot 10^9$  protons per pulse, at 6 m from the target and currently under commissioning [3, 4]. EAR2 was constructed to carry out challenging cross-section measurements with low mass samples, reactions with small cross-sections and/or highly radioactive samples [5, 6, 7, 8, 9]. The neutron flux in EAR2 is  $\sim 50$  times higher than in EAR1, and the neutrons take  $\sim 10$  times less time to arrive at the experimental area. In consequence, the signal-to-background ratio is increased by a factor of  $\sim 500$  when considering the constant room background or the radioactivity of the samples. Accordingly, the counting rate in the detectors is also increased by approximately the same factor, as presented in Fig. 1, which introduces some experimental challenges.

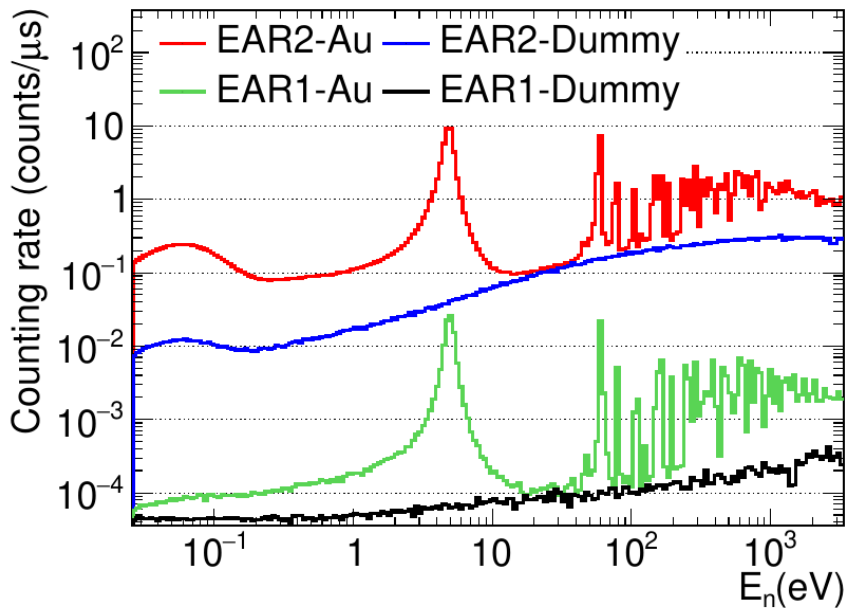


Figure 1 Counting rates obtained as a function of the neutron energy ( $E_n$ ) in the experimental EAR1 (EAR1-Au) and EAR2 (EAR2-Au) for a BICRON detector with a threshold of 0.15 MeV. The detectors are located at 10 cm from a  $^{197}\text{Au}$  sample of 2 cm in diameter and 100  $\mu\text{m}$  thickness. The counting rates of the background obtained when measuring a dummy sample are also presented for the EAR1 (EAR1-Dummy) and the EAR2 (EAR2-Dummy).

Capture cross-section measurements with C6D6 detectors have been performed successfully at n\_TOF EAR1 for almost 20 years [10, 11]. In most cases, the analysis of the C6 D6 detector data was done by applying the Pulse Height Weighting Technique (PHWT) [12, 13, 14], which transforms the

C6 D6 in a Total Energy Detector (TED) [15]. The measurements were performed with commercial BICRON detectors (0.621 liters of C6D6 ) [16] and home-made **de tectors** with carbon-fiber housing (1.0 liters of C6D6 ) [17].

Two capture cross-section measurements have been carried out in EAR2 [9, 18] with these detectors and considerable pile-up effects and gain shifts were observed in the data due to the high counting rates at EAR2 ( $\geq 1$  counts/ $\mu$ s) [19]. These effects increased with the neutron energy (i.e. at shorter times of flight) and required the introduction of considerable corrections in the capture cross-section data analysis. To overcome these limitations, a Segmented Total Energy Detector (sTED) [20] has been developed. It consists of an array of small active volume C6D6 modules coupled to photomultipliers optimized for high counting rates applications.

This report discusses the performance of the large volume C6D6 detectors at EAR2 in Section 2, the properties of the new sTED detector in Section 3, details of its performance at n\_TOF EAR2 in Section 4 and the summary and conclusions of this work in Section 5.

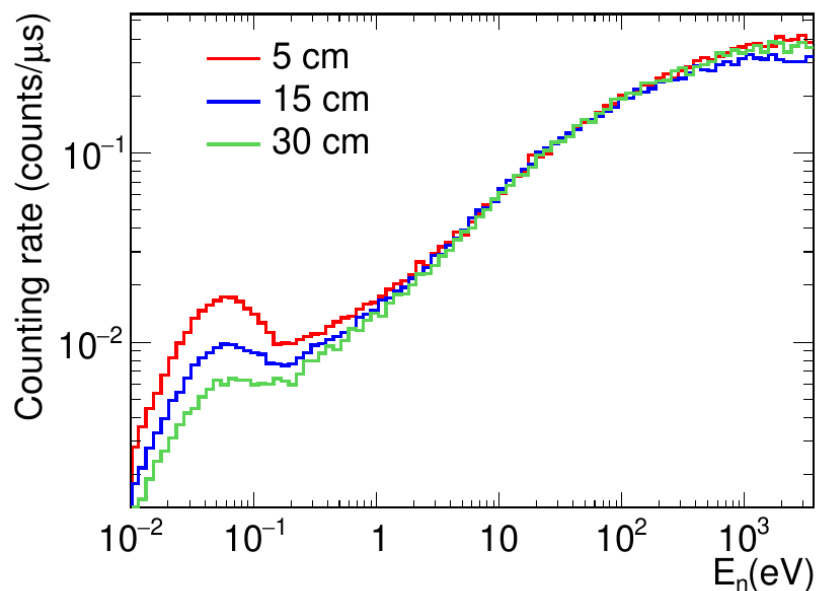


Figure 2 Counting rates obtained for a BICRON detector as a function of the neutron energy ( $E_n$ ) with a 0.15 MeV deposited energy threshold in a beam-on measurement without any sample in place. The measurements are performed with the detector at the same height but at three different distances (5, 15 and 30 cm) from the center of the beam.

## 2 Performance of C<sub>6</sub>D<sub>6</sub> detectors at EAR2

As mentioned previously, the BICRON detectors and the home-made detectors with carbon-fiber housing that have been commonly used at EAR1 stand very high counting rates in capture measurements at EAR2. Hence, the measured data suffer from:

- Pile-up effects. As shown in Fig. 1, the counting rate reaches up to 10 counts per  $\mu$ s or even higher values. Such a high counting rate with the 10 ns Full Width at Half Maximum (FWHM)

signals of the BICRON and carbon-fiber detectors lead to significant pile-up effects. Pulse shape fitting can be used [21] for reconstructing piled up signals, but even with this technique  $\sim 25\%$  of the signals are lost at a counting rate of 10 counts per  $\mu\text{s}$  [19]. One possible solution for reducing the pile-up is to move the C6D6 detectors away from the sample, thus reducing the efficiency and therefore the count rate. However, experimental measurements performed in EAR2 with BICRON detectors have shown that the neutron beam-related background (i.e. counts in the detector without any sample) is almost constant at different distances from the center of the beam for C6D6 detectors, as presented in Fig. 2. Therefore, moving the detectors further away from the sample decreases the signal to beam-related background. Since the beam-related background of experimental EAR2 is one of the main limitations for performing capture measurements there [19, 22], it is not advisable to move the C6 D6 detectors further away from the sample.

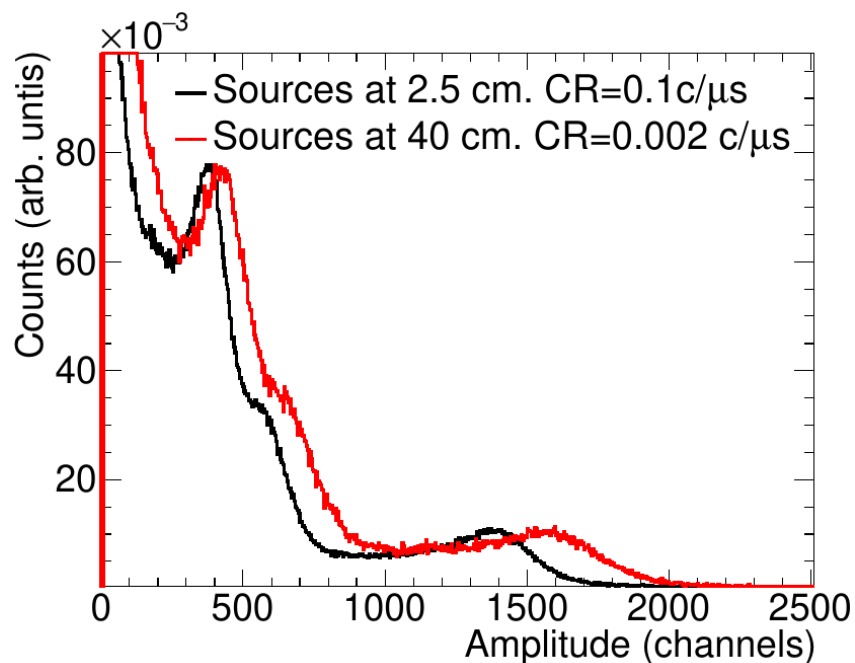


Figure 3 Amplitude spectra for a combination of  $^{137}\text{Cs}$  and  $^{88}\text{Y}$  calibration sources placed at two different distances from a carbon-fiber detector. A gain shift of 12% is observed from one measurement to the other. The Counting Rates (CR) obtained with an energy threshold of 0.15 MeV are also given in the figure.

- Gain shifts that modify the energy calibration. At n\_TOF EAR2, three distinct types of gain shifts have been observed in the C6 D6 detectors: gain shifts due to the high constant counting rates, gain shifts due to the arrival of the ultra-relativistic particles from the spallation target and gain shifts produced by rapid variations of the counting rates as a function of the time of flight. The effects are described in the following list:
  - Gain shifts due to high constant counting rates. They appear when the counting rate in the detector increases from one constant value to a higher constant value and have been observed and characterized in measurements performed with high activity  $\gamma$ -ray calibration sources. Fig. 3 depicts an example of this effect for a carbon-fiber housing detector: the pulse height spectra in the detector recorded with strong  $^{137}\text{Cs}$  and  $^{88}\text{Y}$  sources with a total activity of  $\sim 400$  kBq placed at different

distances (i.e different counting rates) is shifted. As a consequence, they would need a different energy calibration.

- Gain shifts due to the arrival of the ultra-relativistic particle flash in the detectors placed at n\_TOF EAR2. The particle flash arrives at the experimental area at very short times ( $<1 \mu\text{s}$ ) and induces a strong saturation of the detectors. As a result, gain shifts as a function of time of flight (i.e. neutron energy) appear during the recovery of the BICRON and carbon-fiber detectors. The gain of the detectors slowly recovers and after approximately 10 milliseconds (corresponding to neutrons of approximately 0.02 eV) it shows no further change. This effect is presented in Fig. 4, where the deposited energy spectra for a  $^{197}\text{Au}$  sample are shown for different neutron energy ranges. The amplitude spectra should be equal in the energy range of the figure, and thus the visible differences are due to gain shifts produced by the particle flash. In the Figs. 4 and 5, the mass of the Au sample used is low enough (not as in Fig. 1) to exclude pile-up effects in all the spectra shown. In Fig. 5, the deposited energy spectra for three different beam intensities in the same energy range are presented. It can be seen that the gain shift with higher intensity is higher indicating that the effects of the particle flash increase with the beam intensities.

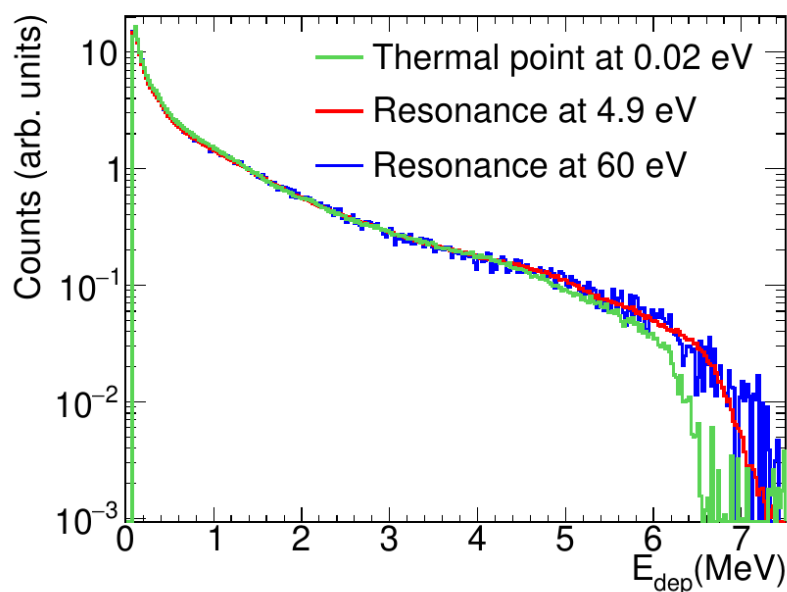


Figure 4 Deposited amplitude spectra obtained a measurement with a BICRON detector at 5 cm from a  $^{197}\text{Au}$  sample of 0.5 cm diameter and  $100 \mu\text{m}$  thickness. The spectra are presented for different neutron energy ranges with a nominal intensity of  $7 \cdot 10^{12}$  protons.

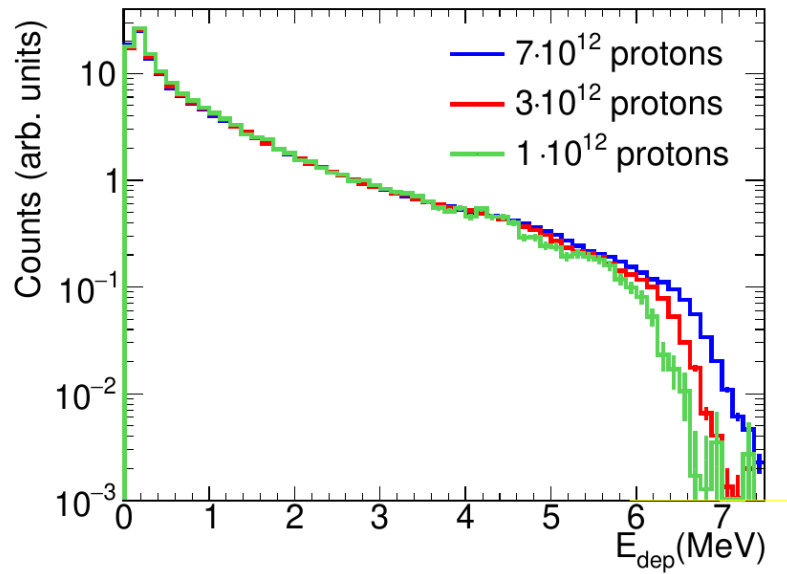


Figure 5 Deposited amplitude spectra obtained for measurements with a BICRON detector at 5 cm from a  $^{197}\text{Au}$  sample of 0.5 cm diameter and 100  $\mu\text{m}$  thickness. The spectra are for the resonance at 4.9 eV for pulses with three different average intensities.

- Gain shifts produced by rapid counting rate variations as a function of the time of flight. It has been observed that the detectors show different gains at neutron energies above and below a strong resonance inducing a high counting rate. As shown in Fig. 6, the gain of the detector at neutron energies in the range 6-8 eV (above the 4.9 eV  $^{197}\text{Au}$  saturated resonance) increases in the range 1.5-3.5 eV, and then recovers gradually at the thermal point. This effect can't be due to pile-up and thus is attributed to a gain shift produced by the high counting rate ( $\sim 10$  counts/ $\mu\text{s}$ ) of the saturated resonance at 4.9 eV.

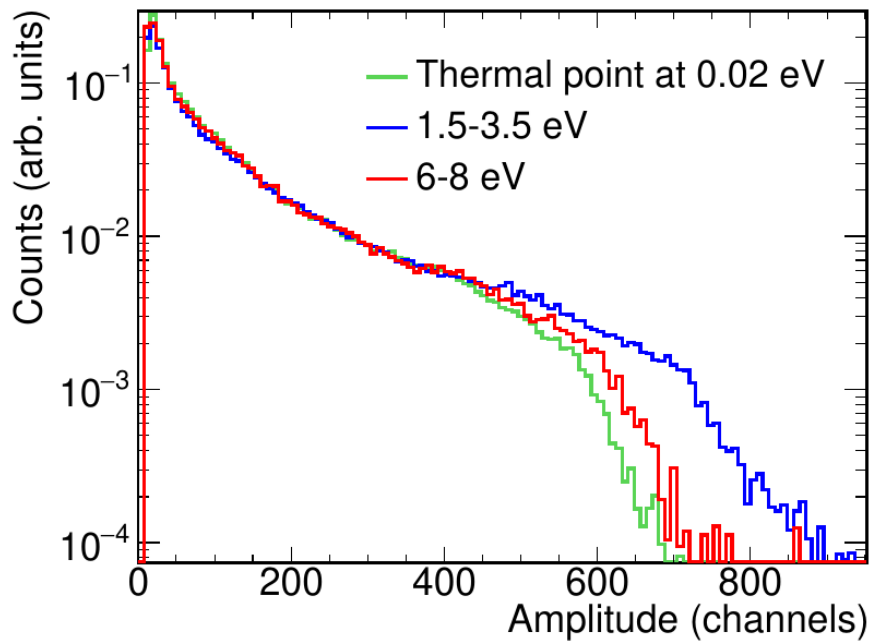


Figure 6 Amplitude spectra obtained for measurements with a carbon-fiber detector at 10 cm from a  $^{197}\text{Au}$  sample of 2 cm diameter and 100  $\mu\text{m}$  thickness. The spectra are presented for different neutron energy ranges.

### 3 sTED description and specifications

The sTED has been specifically designed to improve the capture setup at EAR2, following the simple idea of reducing the counting rate per module in one order of magnitude, by replacing large volume C6D6 detectors with a much larger amount of smaller detectors (modules), forming an array with a comparable total efficiency. Each sTED module has an active volume of 0.044 liters, which is  $\sim 14$  times and  $\sim 23$  times smaller than the active volumes of the BICRON (0.621 liters) and the carbon-fiber (1.0 liters) detectors, respectively. In addition, smaller photomultipliers optimized for high counting rates are used for providing additional robustness. The following subsections present the technical specifications, the detector response to  $\gamma$ -rays, and the application of the PHWT to the data measured with an sTED array.

#### 3.1 Detector characteristics

The sTED module was first designed by Monte Carlo simulations and then characterised at CIEMAT's laboratory. After the successful tests, nine modules were ordered from Scionix [23]. Fig. 7 shows a picture of one module and a possible assembly of 9 modules. The amount of C6D6 liquid in each module is 0.044 liters and it is coupled to the photomultiplier with a quartz window. The dimensions of the module and its elements are presented in Fig. 8.



Figure 7 Picture of one sTED module (top). Picture of 9 sTED modules grouped as a cluster (bottom).

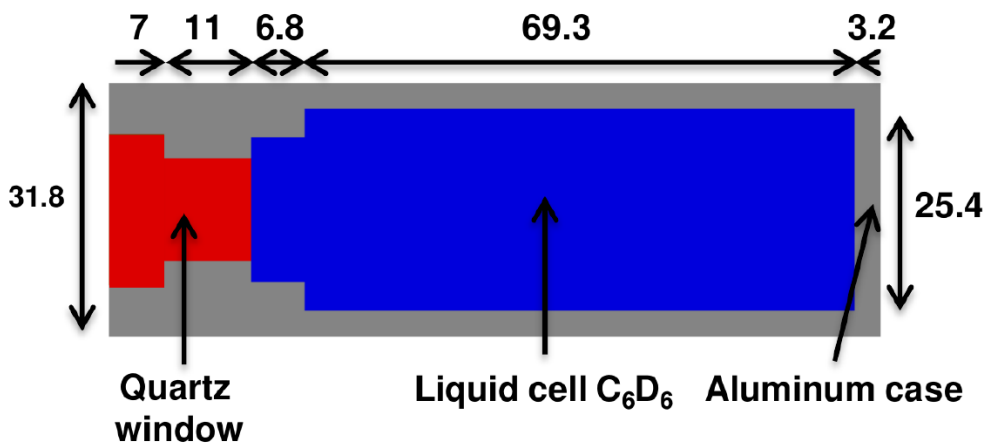


Figure 8 Drawing of one sTED module with the different components and their sizes in millimeters.

Three different 1" Hamamatsu photo-multipliers [24] coupled to an sTED module were tested: R5611A, R2076 and R11265U. It was found that R5611A and R2076 also suffered from gain shifts when exposed to high counting rates of  $\sim 0.05$  counts/ $\mu$ s, whereas the Hamamatsu R11265U 26x26 mm showed a stable gain up to at least 0.25 counts/ $\mu$ s. This photomultiplier has a borosilicate window and Super Bialkali (SBA) photocathodes specially designed for high counting rates.

In addition, we have performed a detailed study of the shape of the sTED signals. As can be seen in Fig. 9, there are two types of signals. The ones with an area-to-amplitude ratio greater than 7.4 are due to  $\gamma$ -rays depositing energy in the scintillation liquid. The remaining signals have a different origin, which was attributed to the instantaneous production of one or a few photo-electrons in the photo-cathodes of the photo-multipliers [25]. These signals are called noise in this work because they are not produced by  $\gamma$ -rays interacting with the C6D6 liquid.

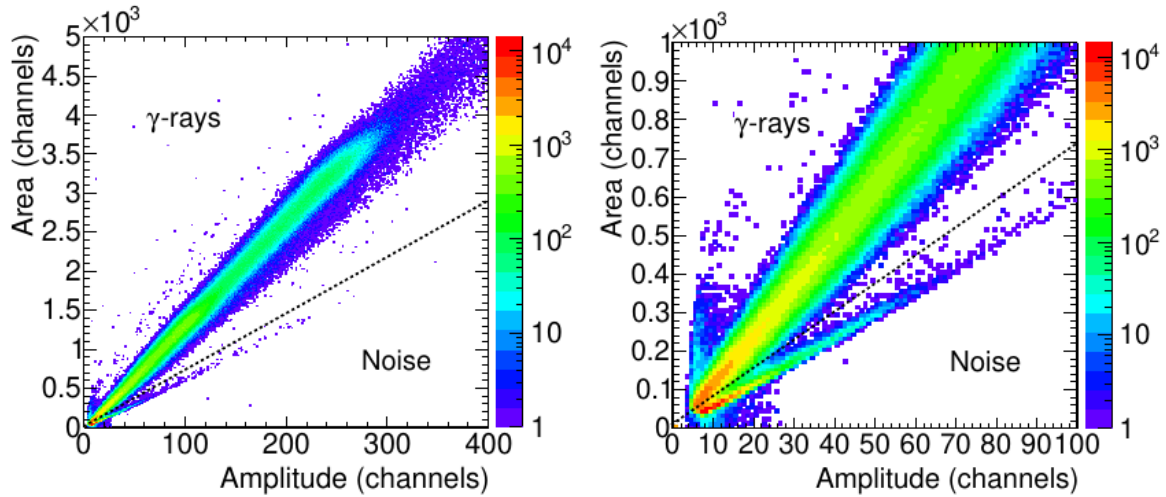


Figure 9 2D plot showing the amplitude versus the area of the sTED signals with a R5611A photomultiplier when measuring an  $^{88}\text{Y}$  calibration source. The black dashed line separates the two different types of signals. The bottom figure is a zoom of the top figure.

At n\_TOF, the signals are digitized, stored, and then analyzed using dedicated pulse shape analysis routines [26]. To mitigate potential pile-up effects in EAR2, pulse shape fitting is found to be the most effective approach [21]. The optimal discrimination between the two types of signals are obtained by utilizing two average signal shapes (depicted in Fig. 10), one for signals related to  $\gamma$ -rays and the other to the noise.

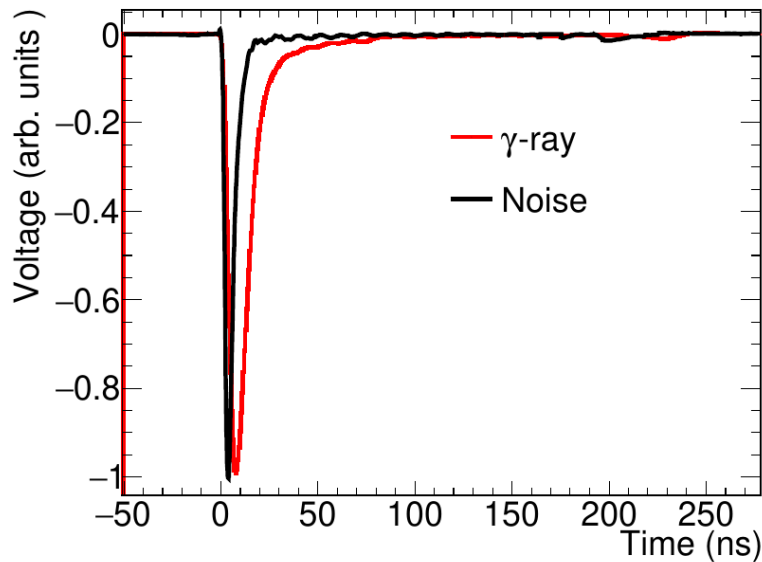


Figure 10 Average sTED signals produced by  $\gamma$ -rays and by the noise.

The time resolution of one sTED module was measured with respect to a  $\text{LaBr}_3$  detector with  $354 \pm 4$  (statistical)  $\pm 10$  (systematic) ps time resolution [27]. The coincident signals corresponding to the detection of the 1173 and 1332 keV  $\gamma$ -rays from a  $^{60}\text{Co}$  source in each detector are used to determine the time resolution, assuming that both detectors have a Gaussian time response. The distribution of the time differences between the coincident sTED and  $\text{LaBr}_3$  events is shown in Fig.

11. The obtained time resolution of an sTED module is  $742 \pm 15$  ps, including both statistical and systematic uncertainties.

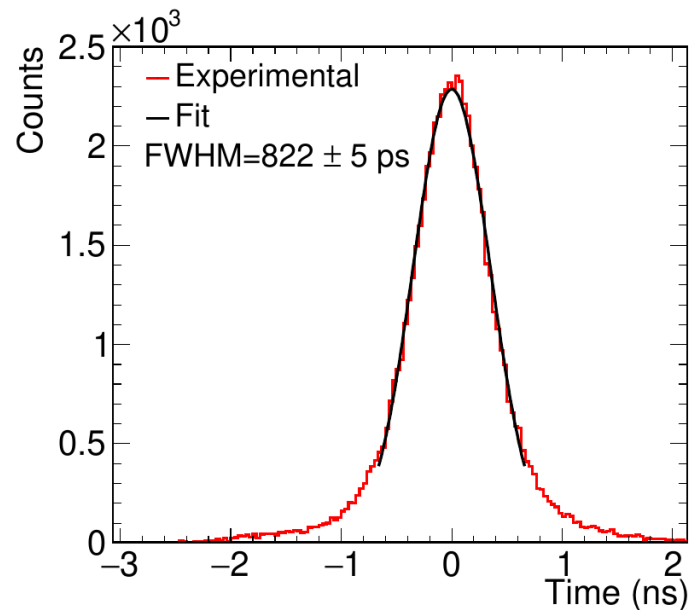


Figure 11 Distribution of the time differences between signals in coincidence between an sTED module and a  $\text{LaBr}_3$  detector, when measuring a  $^{60}\text{Co}$  source. The FWHM of the distribution is  $822 \pm 5$  ps, including the contribution of the  $\text{LaBr}_3$ .

One should notice that the reduction of the active volume and the need of using a solid housing for keeping the liquid scintillator and the use of a PMT with borosilicated glass window (instead of quartz) could have the drawback of increasing the neutron sensitivity [16] compared to larger volume detectors with similar housing thicknesses. The neutron sensitivity of the sTED was estimated by Monte Carlo simulations for capture measurements of various isotopes.

The values are given in Table 1, where the magnitude of the background due to scattered neutrons is estimated for some specific resonance in certain nuclei. There  $E_n$  is the resonance energy;  $\Gamma_n$  and  $\Gamma_\gamma$  are its neutron and radiative widths, respectively;  $\epsilon_n$  is the probability of detecting a neutron scattered in the sample and with energy  $E_n$ ;  $\epsilon_\gamma$  is the efficiency of detecting the corresponding  $(n,\gamma)$  cascade, and  $(\epsilon_n/\epsilon_\gamma)/(\Gamma_n/\Gamma_\gamma)$  estimates the size of the background due to elastic scattered neutrons compared to the  $(n,\gamma)$  detected events.

The values  $(\epsilon_n/\epsilon_\gamma)/(\Gamma_n/\Gamma_\gamma)$  given in Table 1 indicate that the neutron scattering background in the  $^{240}\text{Pu}$ ,  $^{242}\text{Cm}$  and  $^{197}\text{Au}$  are  $\lesssim 0.1\%$ . However, for resonances with unfavorable  $(\Gamma_n/\Gamma_\gamma)$  values like the ones in  $^{207}\text{Pb}$  and  $^{209}\text{Bi}$ , the neutron-induced background would be as large as 8.4% and 24%, respectively, and would require important corrections. For this particular case, highly optimized C6D6 detectors such as the ones with a carbon-fiber housing, thinner optical (or no) windows, and PMTs with quartz windows [16] may be required.

Isotope	En	$\Gamma_n/\Gamma_\gamma$	$\epsilon_n/\epsilon_\gamma$	$(\epsilon_n/\epsilon_\gamma)/(\Gamma_n/\Gamma_\gamma)$
$^{240}\text{Pu}$	5.01 eV	$8.4 \cdot 10^{-2}$	$1.6 \cdot 10^{-3}$	$1.6 \cdot 10^{-3}$
$^{240}\text{Pu}$	1.35 keV	8.5	8.5	8.5
$^{244}\text{Cm}$	7.66 eV	4.9	4.9	4.9
$^{244}\text{Cm}$	86.1 eV	$6.6 \cdot 10^{-1}$	$6.6 \cdot 10^{-1}$	$6.6 \cdot 10^{-1}$
$^{197}\text{Au}$	4.91 eV	$1.2 \cdot 10^{-1}$	$1.2 \cdot 10^{-1}$	$1.2 \cdot 10^{-1}$
$^{207}\text{Pb}$	41.1 keV	$3.7 \cdot 10^2$	$3.7 \cdot 10^2$	$3.7 \cdot 10^2$
$^{207}\text{Bi}$	12.1 keV	$2.2 \cdot 10^3$	$2.2 \cdot 10^3$	$2.2 \cdot 10^3$

Table 1 Estimation of the neutron sensitivities  $((\epsilon_n/\epsilon_\gamma)/(\Gamma_n/\Gamma_\gamma))$  of the sTED for different nuclei and resonances. The details of the table can be found in the body text.

### 3.2 Detector response to $\gamma$ -rays

As described in section 2, the BICRON and carbon-fiber detectors exhibited gain shifts when exposed to high activity  $\gamma$ -ray calibration sources. The response of the sTED modules was investigated with a 20 MBq  $^{137}\text{Cs}$  source placed at different distances from the detector. The comparison of the  $^{137}\text{Cs}$  pulse height spectra recorded at 0.25,  $2 \cdot 10^{-2}$  and  $1.5 \cdot 10^{-3}$  c/ $\mu\text{s}$  are shown in Fig. 12. It can be concluded that for counting rates as large as 0.25 c/ $\mu\text{s}$  no gain shifts are observed.

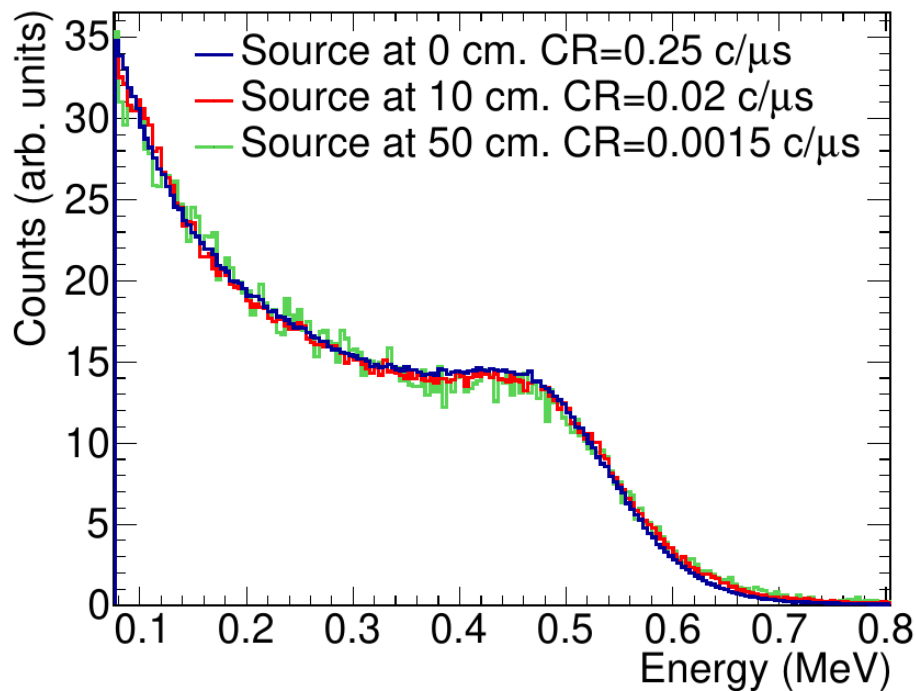


Figure 12 Deposited energy spectra for a 20 MBq  $^{137}\text{Cs}$  calibration source placed at different distances from an sTED module with a R5611A photomultiplier, along with the Counting Rates (CR) obtained using a deposited energy threshold of 0.15 MeV.

The linearity and the energy resolution of the detector were characterized with six  $\gamma$ -ray sources:  $^{133}\text{Ba}$ ,  $^{137}\text{Cs}$ ,  $^{207}\text{Bi}$ ,  $^{60}\text{Co}$ ,  $^{88}\text{Y}$  and AmBe. The procedure used consisted of:

- Gaussian folding of the Monte Carlo spectra.
- Re-calibration of the experimental data.

- Variation of the Gaussian folding and energy calibration parameters, until the best fit of the experimental Compton edge distributions to the Monte Carlo simulated ones is reached.
- Determination of the centroids of the Compton edges and the resolution ( $\Delta E/E$ ). Hereafter,  $E$  is the deposited energy in the detectors.
- Least squares fit of the Compton edge centroids to linear and parabolic energy calibrations, for determining the energy calibration curve.
- Fit of the  $\Delta E/E$  values to the  $\Delta E/E=2.35\cdot\sqrt{(\alpha\cdot E+\beta\cdot E^2)}/E$  resolution function, for determining the energy resolution as a function of deposited energy  $E$ .

In order to perform the sTED calibration with the described procedure, Monte Carlo simulations have been performed with a detailed geometric description of the sTED modules and the well-validated Standard Electromagnetic physics package of Geant4 [28].

The top panel of Fig. 13 shows the least square fits of linear and parabolic functions to the experimental centroids of the Compton edges for the different  $\gamma$ -ray energies. It can be seen from the coefficients of determination ( $R^2$ ) that the linear and parabolic curves reproduce with equal accuracy the data and hence the calibration can be assumed to be linear. The fit of the detector energy resolution is presented in the bottom panel of Fig. 13. The result of this fit is  $\Delta E/E=2.35\cdot\sqrt{(\alpha\cdot E+\beta\cdot E^2)}/E= 2.35\cdot\sqrt{(0.00545\cdot E+0.000729\cdot E^2)}/E$ , which provides resolution values for this detector of 18% at 1 MeV and 10% at 10 MeV. The excellent agreement between the experimental and simulated spectra for the six  $\gamma$ -ray sources are shown in Fig. 14, indicating the high quality of the energy calibration and energy resolution determination. The differences for the AmBe spectra below the Compton edge are related to the response to the neutrons, which was not simulated.

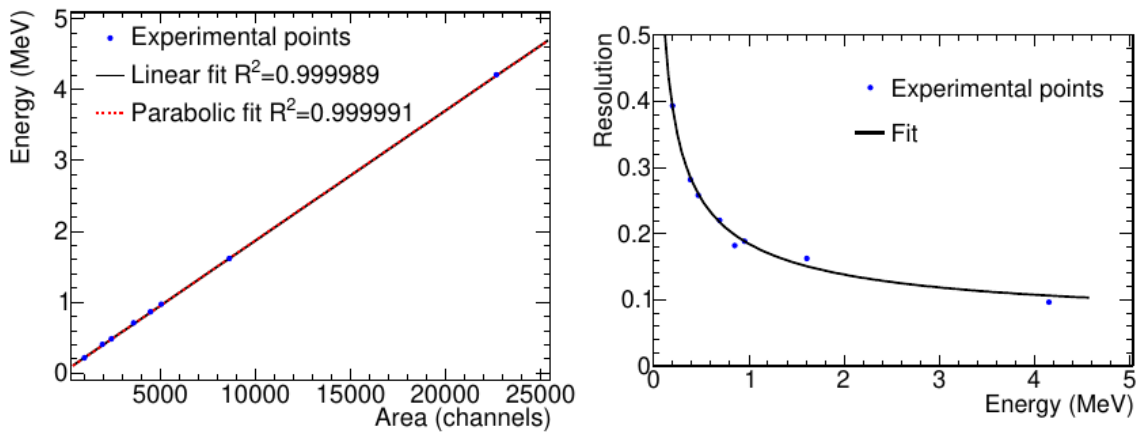


Figure 13 Top panel: deposited energy in the detector as a function of the area of the signals (blue points). The values have been fitted to a straight line (black dashed line) and a parabola (red dashed line). Bottom panel: energy resolution of one sTED module as a function of the deposited energy (blue points). The experimental points have been fitted to the function:  $\Delta E/E=2.35\cdot\sqrt{(\alpha\cdot E+\beta\cdot E^2)}/E$ .

It is also important to notice that the Monte Carlo simulations are also used in the experimental technique applied in the analysis of  $(n,\gamma)$  cross-section measurements, as described in detail in

Section 3.3. For this reason, the overall quality of the simulations has been assessed with a measurement of a well-characterized  $^{88}\text{Y}$  source ( $44.3 \pm 1.3$  kBq) at  $5.0 \pm 0.1$  cm to an sTED module.

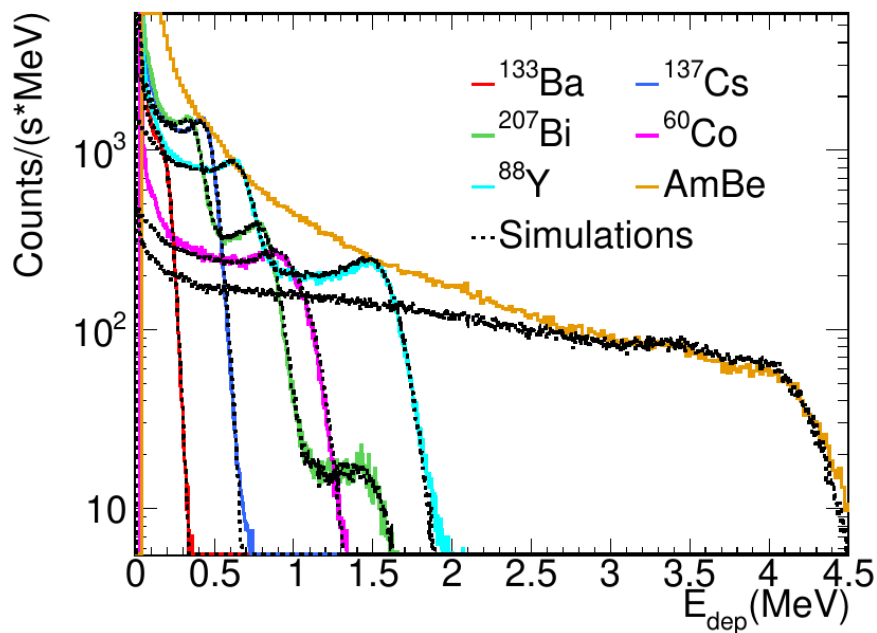


Figure 14 Experimental deposited energy spectra obtained with an sTED module for various  $\gamma$ -ray sources ( $^{133}\text{Ba}$ ,  $^{137}\text{Cs}$ ,  $^{207}\text{Bi}$ ,  $^{60}\text{Co}$ ,  $^{88}\text{Y}$  and AmBe) compared with Geant4 simulations. The simulated spectra are normalized to the experimental ones.

As it can be seen in Fig. 15, the Geant4 simulations folded with the energy resolution reproduce very accurately the area and shape of the experimental response. These Geant4 simulations have been used to determine the efficiency to detect the  $\gamma$ -ray decay of an  $^{88}\text{Y}$  source and other decays. The efficiencies are presented in Table 2 for the sTED, the BICRON, and the carbon-fiber detectors placed at 5 cm from the  $\gamma$ -ray emission point.

	$^{137}\text{Cs}$ decay	$^{88}\text{Y}$ decay	$^{197}\text{Au}(n,\gamma)$ cascade	$^{240}\text{Pu}(n,\gamma)$ cascade
<b>Carbon-fiber</b>	2.87	2.87	2.87	2.87
<b>BICRON</b>	2.28	2.28	2.28	2.28
<b>sTED mod.</b>	0.20	0.20	0.20	0.20

Table 2 Detection efficiencies, expressed as percentages, for three detectors. The efficiencies are for the detection of the  $\gamma$ -ray decay of  $^{137}\text{Cs}$  and  $^{88}\text{Y}$ , as well as for the  $(n,\gamma)$  cascades of  $^{197}\text{Au}$  and  $^{240}\text{Pu}$  computed with the NuDEX code [22, 29]. The efficiencies were calculated with Monte Carlo simulations by simulating the detectors at 5 cm from the  $\gamma$ -ray emission point and for a deposited energy threshold of 0.15 MeV.

### 3.3 The pulse height weighting technique

The sTED has been designed to measure capture cross-sections using the Pulse Height Weighting Technique (PHWT) [12, 13], in which the efficiency of the detection system is transformed to become proportional to the total energy of the  $(n,\gamma)$  cascade, and therefore independent of the de-

excitation pattern. The main conditions to be fulfilled for the applicability of this technique are: the  $\gamma$ -ray detection efficiency ( $\epsilon_\gamma$ ) is low, i.e.  $\epsilon_\gamma \ll 1$ , and proportional to the energy of the  $\gamma$ -ray ( $E_\gamma$ ), i.e.:  $\epsilon_\gamma(E_\gamma)=k \cdot E_\gamma$ . For many detectors, such as the sTED, the efficiency to detect a  $\gamma$ -ray is not proportional to its energy. In these cases, an “a posteriori” manipulation of the detector response function can be applied to make the detector response proportional to the energy of the  $\gamma$ -rays [12, 13]. This is done by applying a weight to each recorded count dependent on its energy (pulse height), calculated from the so-called Weighting Function (WF).

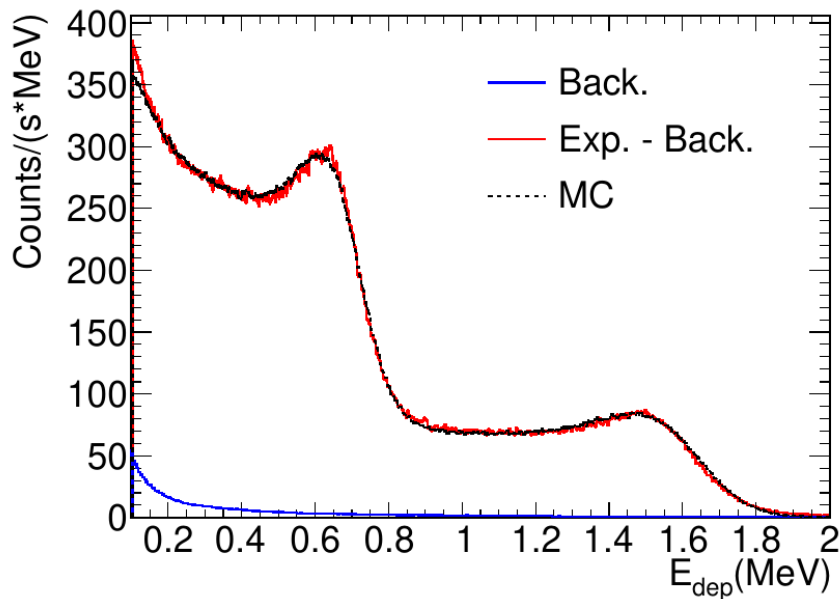


Figure 15 Deposited experimental energy spectra (Exp.-Back.) after subtracting the background (Back.) for an  $^{88}\text{Y}$   $\gamma$ -ray sources of  $44.3 \pm 1.3$  kBq compared with MC simulations (MC). The MC simulations have been scaled by 1.03 to normalize to the experimental results. The uncertainty in the activity of the  $^{88}\text{Y}$   $\gamma$ -ray source is 3% so it is compatible with the scaled value.

For the case of an array of many sTED modules, the total  $\gamma$ -ray detection efficiency of the setup can increase considerably. However, the PHWT can be still used to obtain the capture cross-section as presented in reference [22], as long as the intrinsic efficiency of each module remains small ( $\epsilon_\gamma \ll 1$ ). For the case of one sTED module, the efficiency to detect  $\gamma$ -rays from the (n, $\gamma$ ) cascades that are in the order of a few MeVs is low enough due to its small active volume.

In order to apply the PHWT, the WF has to be calculated for each setup. As described in reference [13], the best known method for determining this function is to use accurate Monte Carlo simulations including a detailed geometrical description of the full experimental setup. For this reason, in Section 3.2 the Monte Carlo simulations of an sTED module have been validated. The WF for a setup consisting of three sTED modules has been calculated. This particular setup was utilized to determine the capture yield of  $^{197}\text{Au}$  in EAR2, as explained in Section 4. The detector response of the setup was obtained through detailed Monte Carlo simulations, as depicted in Fig. 16. The simulation results were then fitted to derive a WF parameterized as a 5th-degree polynomial for each sTED module, following the procedure described in [13]. A plot of one of these WFs can be observed in Fig. 17.

The verification of the polynomial WF being able to transform the detector efficiency of a  $\gamma$ -ray proportional to his energy have been done simulating  $\gamma$ -rays of 150 energies. For each  $\gamma$ -ray energy, the efficiency to detect it by applying the WF has been divided by his energy, resulting in a number defined as Q-factor which should be equal to one. The small deviations of the Q-factors from one in Fig. 18 demonstrate the high accuracy of the method by applying the smooth WF described by a 5th-degree polynomial.

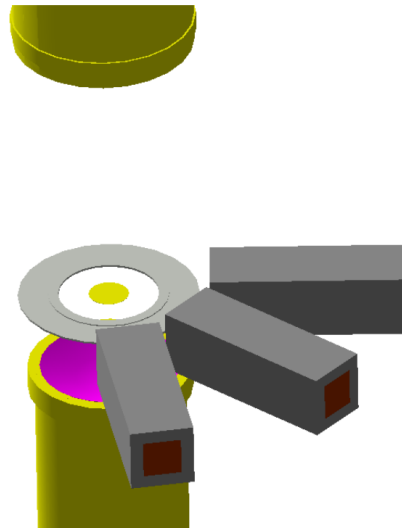


Figure 16 Image of the setup simulated in Geant4 with three sTED modules and the gold sample. The sTED module number one is located at the left of the figure, number two in the middle and three at the right.

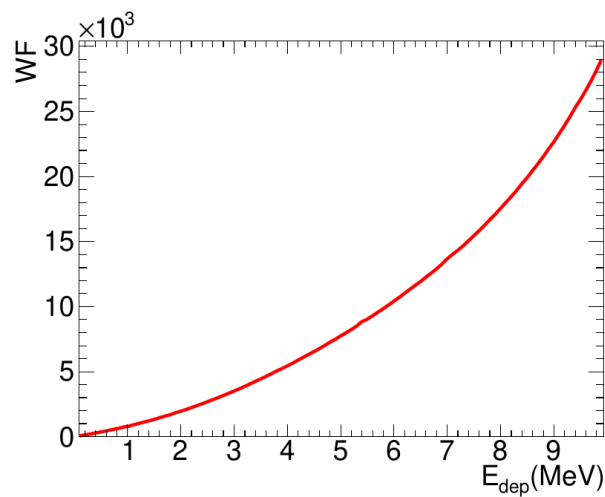


Figure 17 Weighting function for sTED number one.  $WF(E) = 6.5071 + 656.261 \cdot E + 113.929 \cdot E^2 + 34.5488 \cdot E^3 - 6.39125 \cdot E^4 + 0.411521 \cdot E^5$ , the energy is set in MeV.

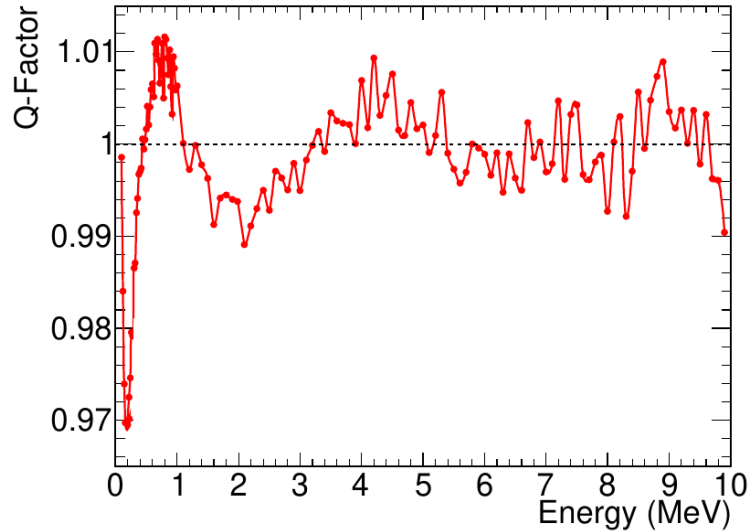


Figure 18 Q-factor determined for 150  $\gamma$ -ray energies.

#### 4 Experimental validation at n\_TOF EAR2

Due to the challenging conditions for performing capture measurements at n\_TOF EAR2 described in Section 2, the most reasonable method to validate the sTED is to perform a capture experiment and compare the results with the evaluated cross section data. A suitable isotope for this purpose is  $^{197}\text{Au}$ , which can be obtained in high-purity metallic samples and has a standard capture cross-section at thermal energy and between 0.2 and 2.5 MeV [30]. In addition,  $^{197}\text{Au}$  has been measured many times at n\_TOF as a reference or in a dedicated campaign [31,32]. In 2022, a capture measurement was carried out with three sTED modules placed horizontally at 5 cm from the center of a 2 cm diameter and 0.1 mm thickness  $^{197}\text{Au}$  sample. Fig. 16 shows a scheme of the setup.

In addition to the capture yield, the deposited energy spectra measured for (n, $\gamma$ ) reactions in  $^{197}\text{Au}$  were compared with simulations performed with Geant4 in Fig. 19. The  $\gamma$ -cascades used in the simulations were obtained by fitting the Total Absorption Calorimeter (TAC) data [33,34] and have been used in other experimental measurements [19, 35,36]. The agreement between the shape of the experimental cascade and the one obtained from simulations indicates that there are no significant gain shifts in the detector when it is used for time-of-flight measurements at EAR2.

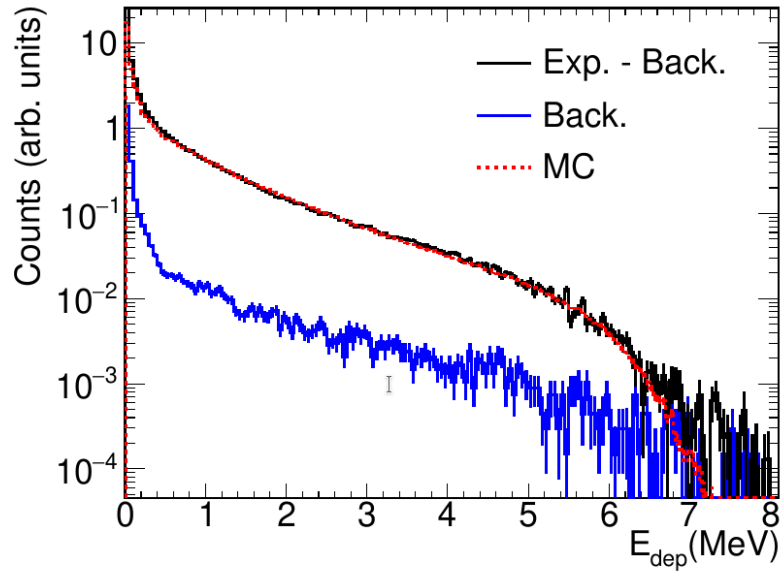


Figure 19 Experimental deposited energy spectra in one sTED module (Exp.-Back.) with background subtracted (Back.) and simulated with Geant4 (MC) for  $^{197}\text{Au}(n,\gamma)$  cascades.

The capture yield has been determined by applying the WF calculated in Section 3.3 to obtain the weighted counting rate as a function of the neutron energy and dividing it by the neutron fluence of the EAR2, after subtracting the different background components. The experimental yield was compared with the yield obtained with the JEFF-3.3 [37] cross-section broadened with the Resolution Function (RF) of the EAR2 [38, 39]. The comparison, normalized in the region between 0.01 and 1 eV, is presented in Figs. 20 and 21. As it can be observed, the yields are very similar below 500 keV, that correspond to neutrons that are at  $\sim 2 \mu\text{s}$  from the strong EAR2 particle flash. The small differences observed are attributed to uncertainties in the preliminary fluence shape or RF [39]. At energies higher than 500 keV, there are considerable differences, which are attributed to the opening of the (n,np) inelastic reaction channels at 100 keV, that has not been considered in the analysis. The main conclusion of the analysis is that the sTED detectors are capable of measuring a capture cross section up to (at least) 500 keV without suffering any degradation of its performance and thus are an excellent tool for exploiting the high intensity neutron beam of EAR2.

The sTED detector has already been used at n\_TOF EAR2 to perform capture measurements of different isotopes ( $^{79}\text{Se}$ ,  $^{94}\text{Nb}$ ,  $^{160}\text{Gd}$  and  $^{94,95,96}\text{Mo}$ ) in various geometric configurations, producing very promising data [40,41, 42, 43,44].

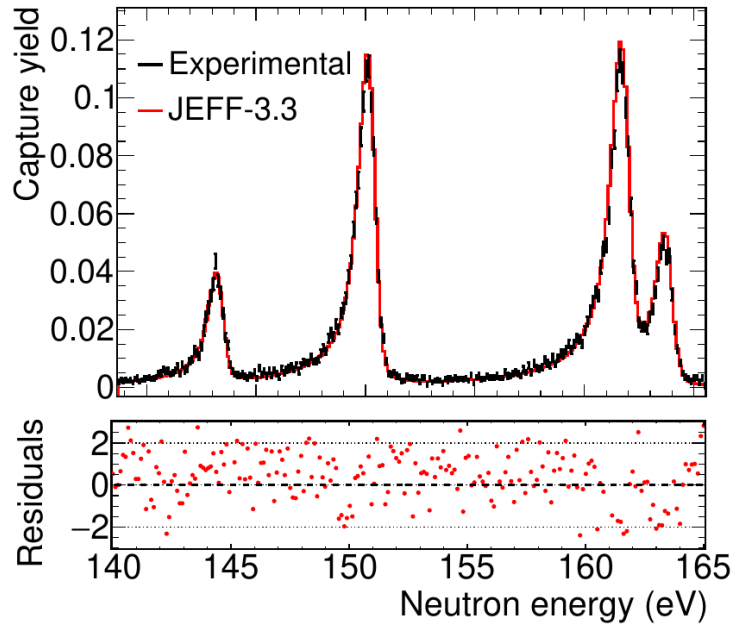


Figure 20 sTED Experimental capture yield obtained with a  $^{197}\text{Au}$  sample (Experimental) compared with the yield obtained from the JEFF-3.3 nuclear data library (Evaluation) in the energy region between 140 and 165 eV. In the bottom panel of the figure, the residuals are plotted. Error bars are due to uncertainties due to counting statistics only.

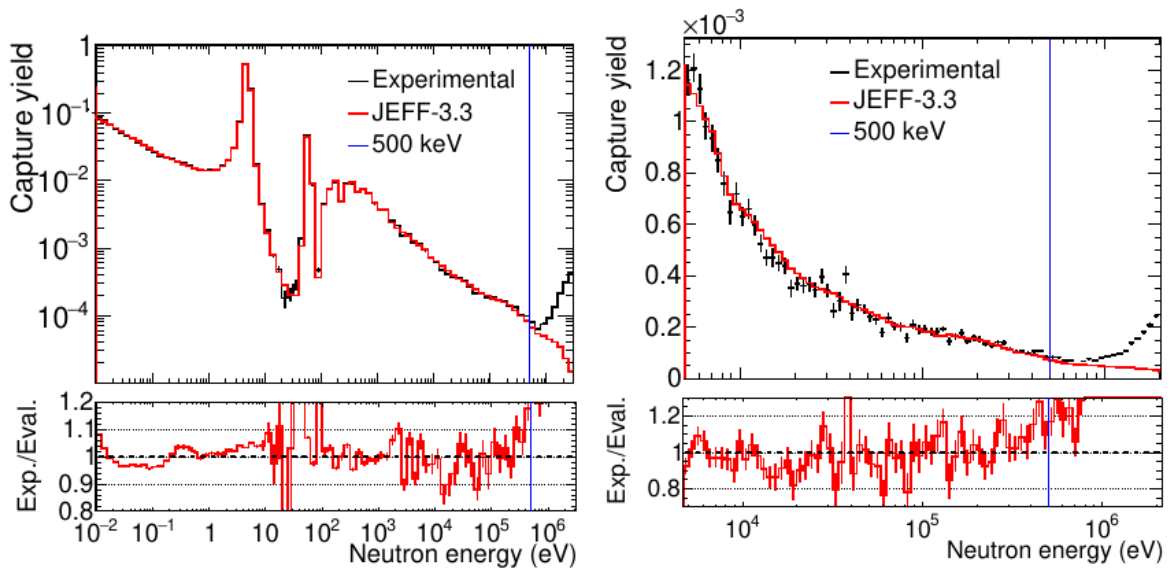


Figure 21 sTED experimental capture yield obtained with a  $^{197}\text{Au}$  sample (Experimental) compared with the yield obtained for the JEFF-3.3 nuclear data library (Evaluation). The top figure has ten bins per decade and the bottom one thirty bins per decade. In the bottom panels, the ratios between the two yields are presented. Error bars are due to uncertainties due to counting statistics only.

## 5 Summary and conclusions

The performance of C6D6 detectors at n\_TOF EAR2 for capture measurements, has been discussed. An alternative segmented Total Energy Detector (sTED), also based on the C6D6 liquid scintillator, has been developed for improving the response of the large volume detectors to the high counting rates.

This has been achieved by an array of smaller active volume modules coupled to photo-multipliers optimized for high counting rates. The performance of the sTED detector in capture measurements with the PHWT is described:

- The main characteristics of the sTED have been determined experimentally, showing that the detector is linear in the entire energy range considered.
- The response of the sTED modules to  $\gamma$ -rays has been validated with Monte Carlo simulations and measurements with well characterised  $\gamma$ -ray sources.
- The applicability of the PHWT has been validated by Monte Carlo simulations, by verifying that a smooth WF is capable of producing a weighted efficiency proportional to the  $\gamma$ -ray energy.

Last, but not least, an experimental campaign was carried out for validating the sTED under the demanding conditions of the n\_TOF EAR2. The experimental capture yield obtained for a  $^{197}\text{Au}$  sample was compared to the the JEFF-3.3 capture cross-section, showing an excellent agreement. The data show that the detector is capable of measuring a capture cross-section at EAR2 up to (at least) 500 keV, which is far above the 1-10 keV limit reached with large volume C6D6. The sTED has been used already in several experimental campaigns.

## 6 References

- [1] C. Guerrero, et al. (The n\_TOF Collaboration), *Eur. Phys. J. A* 49 (2013) 27. doi:10.1140/epja/i2013-13027-6.
- [2] C. Weiss, et al. (The n\_TOF Collaboration), *Nucl. Instrum. Methods A* 799 (2015) 90–98. doi:10.1016/j.nima.2015.07.027.
- [3] M. Ferrari, et al., *Phys. Rev. Acc. and Be.* 25 (2022). doi:10.1103/PhysRevAccelBeams.25.103001.
- [4] Gervino, et al., *Universe* 8 (2022). URL: <https://www.mdpi.com/2218-1997/8/5/255>. doi:10.3390/universe8050255.
- [5] M. Barbagallo, et al. (The n\_TOF Collaboration), *Phys. Rev. Lett.* 117 (2016) 152701. doi:10.1103/PhysRevLett.117.152701.
- [6] Sabaté-Gilarte, et al., *EPJ Web Conf.* 146 (2017) 08004. doi:10.1051/epjconf/201714608004.
- [7] L. Damone, et al. (The n\_TOF Collaboration), *Phys. Rev. Lett.* 121 (2018) 042701. doi:10.1103/PhysRevLett.121.042701.
- [8] A. Stamatopoulos, et al. (n\_TOF Collaboration), *Phys. Rev. C* 102 (2020) 014616. doi:10.1103/PhysRevC.102.014616.
- [9] V. Alcayne, et al., *EPJ Web Conf.* 239 (2020) 01034. doi:10.1051/epjconf/202023901034.
- [10] C. Guerrero, et al. (The n\_TOF Collaboration), *Nuclear Data Sheets* 119 (2014) 5–9. doi:https://doi.org/10.1016/j.nds.2014.08.004.

- [11] F. Gunsing, et al. (The n\_TOF Collaboration), EPJ Web Conf. 146 (2017) 11002. doi:10.1051/epjconf/201714611002.
- [12] R. L. Macklin, J. H. Gibbons, Phys. Rev. C 159 (1967) 1007. doi:10.1103/PhysRev.159.1007.
- [13] U. Abbondanno, et al. (The n\_TOF Collaboration), Nucl. Instrum. Methods A 521 (2004) 454–467. doi:10.1016/j.nima.2003.09.066.
- [14] A. Borella, et al., Nucl. Instrum. Methods A 577 (2007) 626–640. doi:10.1016/j.nima.2007.03.034.
- [15] M. Moxon, E. Rae, Nucl. Instrum. Methods 24 (1963) 445–455. doi:10.1016/0029-554X(63)90364-1.
- [16] R. Plag, et al., Nucl. Instrum. Methods A 496 (2003) 425–436. doi:10.1016/s0168-9002(02)01749-7.
- [17] P. Mastinu, et al., New C6D6 detectors: reduced neutron sensitivity and improved safety, Technical Report, 2013. URL: <https://cdsweb.cern.ch/record/1558147/>.
- [18] A. Oprea, et al., EPJ Web Conf. 239 (2020) 01009. doi:10.1051/epjconf/202023901009.
- [19] V. Alcayne, Measurement of the  $^{244}\text{Cm}$ ,  $^{246}\text{Cm}$  and  $^{248}\text{Cm}$  neutron induced capture cross sections at the CERN n\_TOF facility, Ph.D. thesis, 2022. URL: <https://cds.cern.ch/record/2811791>.
- [20] V. Alcayne, et al., EPJ Web of Conf. 284 (2023) 01043. doi:10.1051/epjconf/202328401043.
- [21] C. Guerrero, et al., Nucl. Instrum. Methods A 597 (2008) 212–218. doi:10.1016/j.nima.2008.09.017.
- [22] E. Mendoza, et al., Nucl. Instrum. Methods A (2023) 167894. doi:10.1016/j.nima.2022.167894.
- [23] Scionix, 2022. URL: <https://scionix.nl>.
- [24] Hamamatsu, 2022. URL: <https://www.hamamatsu.com/>.
- [25] G. Knoll, Radiation Detection and Measurement, number v. 415 in Radiation Detection and Measurement, Wiley, 1979.
- [26] Žugec, et al. (The n\_TOF Collaboration), Nucl. Instrum. Methods A 812 (2016) 134–144. doi:10.1016/j.nima.2015.12.054.
- [27] P. Gramage, Characterization of large-scale LaBr 3 detectors volume for gamma spectroscopy, Master’s thesis, 2016.
- [28] S. Agostinelli, et al. (the GEANT4 Collaboration), Nucl. Instrum. Methods A 506 (2003) 250–303. doi:10.1016/S0168-9002(03)01368-8.
- [29] E. Mendoza, et al., EPJ Web Conf. 239 (2020) 17006. doi:10.1051/epjconf/202023917006.
- [30] A. Carlson, et al., Nucl. Data Sheets 110 (2009) 3215–3324. doi:10.1016/j.nds.2009.11.001, special Issue on Nuclear Reaction Data.

- [31] C. Massimi, et al. (n\_TOF Collaboration), Phys. Rev. C 81 (2010) 044616. doi:10.1103/PhysRevC.81.044616.
- [32] C. Lederer, et al. (n\_TOF Collaboration), Phys. Rev. C 83 (2011) 034608. doi:10.1103/PhysRevC.83.034608.
- [33] C. Guerrero, et al., Nucl. Instrum. Methods A 608 (2009) 424–433. doi:10.1016/j.nima.2009.07.025.
- [34] C. Guerrero, et al., Nucl. Instrum. Methods A 671 (2012) 108–117. doi:10.1016/j.nima.2011.12.046.
- [35] E. Mendoza, et al. (n\_TOF Collaboration), Phys. Rev. C 90 (2014) 034608. doi:10.1103/PhysRevC.90.034608.
- [36] E. Mendoza, et al. (n\_TOF Collaboration), Phys. Rev. C 97 (2018) 054616. doi:10.1103/PhysRevC.97.054616.
- [37] Data Bank. JEFF-3.3, Technical Report, OECD/NEA, 2017.
- [38] V. Vlachoudis, et al., On the resolution function of the n\_TOF facility: a comprehensive study and user guide, Technical Report, 2021. URL: <https://cds.cern.ch/record/2764434>.
- [39] J. A. Pavón-Rodríguez, et al., EPJ Web of Conf. 284 (2023) 06006. doi:10.1051/epjconf/202328406006.
- [40] J. Lerendegui-Marco, et al., EPJ Web of Conf. 284 (2023) 01028. doi:10.1051/epjconf/202328401028.
- [41] C. Domingo-Pardo, et al., Eur. Phys. J. A 59 (2023) 8. doi:10.1140/epja/s10050-022-00876-7.
- [42] J. Balibrea-Correa, et al., EPJ Web Conf. 279 (2023) 06004. doi:10.1051/epjconf/202327906004.
- [43] M. Mastromarco, et al., EPJ Web of Conf. 284 (2023) 09002. doi:10.1051/epjconf/202328409002.
- [44] R. Mucciola, et al., EPJ Web of Conf. 284 (2023) 01031. doi:10.1051/epjconf/202328401031.

## PART II: Technique of Compton imaging in\_TOF neutron-capture cross-section measurements for background rejection in high count-rate conditions

C. Domingo-Pardo<sup>a</sup> , F. Calvino<sup>b</sup> , J. Balibrea-Correa<sup>a</sup>, V. Babiano-Suarez<sup>a,b</sup>, A. Casanovas<sup>b</sup>, G. Cortes<sup>b</sup>, J. Leredegui-Marco<sup>a</sup>, and A. Tarifeño-Saldivia<sup>a</sup>.

<sup>a</sup>*Instituto de Física Corpuscular, CSIC - Universidad de Valencia, Spain.*

<sup>b</sup>*Universitat Politècnica de Catalunya, Spain.*

# 1 Objectives

Explore the possibility to implement the technique of Compton imaging at n\_TOF neutron-capture cross-section measurements for background rejection in high count-rate conditions.

Sub-objectives:

- Perform measurements in realistic conditions at n\_TOF EAR2 with a dedicated detection system in order to determine its performance for TOF experiments in high count-rate conditions
- Study the behaviour of the system in the laboratory with calibrated sources, in order to characterize the system performance and properly interpret its dead-time and count-rate capabilities
- Explore solutions to mitigate dead-time effects in this type of detection systems

# 2 Methodology

A series of measurements were carried out both at CERN n\_TOF EAR2 and in the laboratory, in order to operate the detection system in high count-rate conditions and explore the maximum count-rate conditions that can be achieved with an i-TED detector. Before describing these measurements, the detection technique and apparatus will be introduced.

## 2.1 Detection technique:

For exploiting gamma-ray imaging in capture TOF experiments an i-TED Compton camera was used. i-TED consists of a Compton imager based on two detection planes that are operated in time coincidence (100 ns). Each detection plane contains position-sensitive detectors (PSDs), which allow one to measure both energy and position of each gamma-ray interaction in the detector. By means of the Compton scattering law, one can obtain information on the incoming radiation direction which, in turn, can be exploited to reject gamma-ray events that did not arise from the position of the sample under study. More details on this measuring concept can be found in Ref [1]. For the determination of the Compton angle, it is assumed that the full gamma-ray energy is deposited in the two detection planes, as shown by the formula below.

$$\cos \theta = 1 + \frac{511}{E} - \frac{511}{E'}$$
$$\delta \theta = \frac{E}{\sin \theta} \left( \frac{1}{E'^2} \left( \frac{\delta E'}{E'} \right)^2 + 2 \sin^2 \theta \left( \frac{\delta r}{r} \right)^2 \right)^{1/2}$$

The latter expression represents the uncertainty on the scattering angle, which depends on the scattering angle itself, the energy resolution of the detection system and its position resolution. As depicted in the following paragraph, high energy and position resolutions are therefore mandatory for applying this technique. In the present work, these conditions were met by combining inorganic scintillation crystals with pixelated silicon photomultipliers (SiPMs).

## 2.2 Description of the detection apparatus:

The system consists of two detection planes regarded as scatterer (S-) and absorber (A-) detectors (see Figure 1). All of them are based on  $\text{LaCl}_3(\text{Ce})$  scintillators, with a size of  $50 \times 50 \text{ mm}^2$ , being the S- and the A- detectors 15 mm and 25 mm thick, respectively. In order to enhance detection efficiency, the A-detector consists of an array of four coplanar detectors. Each crystal is readout by means of an  $8 \times 8$  pixellated SiPM from SensL (OnSemi). All SiPM signals are readout by means of TOFPET2 ASIC chips, developed by PETSys Electronics for Positron-Emission Tomography (PET) medical applications [2]. The 3D-location of the gamma-ray interaction points is achieved by means of customized position-reconstruction algorithms that were developed in previous works [3,4]. More details on the hardware aspects can be found in Ref. [5]. The background rejection capability of the system is reported in Ref. [6].

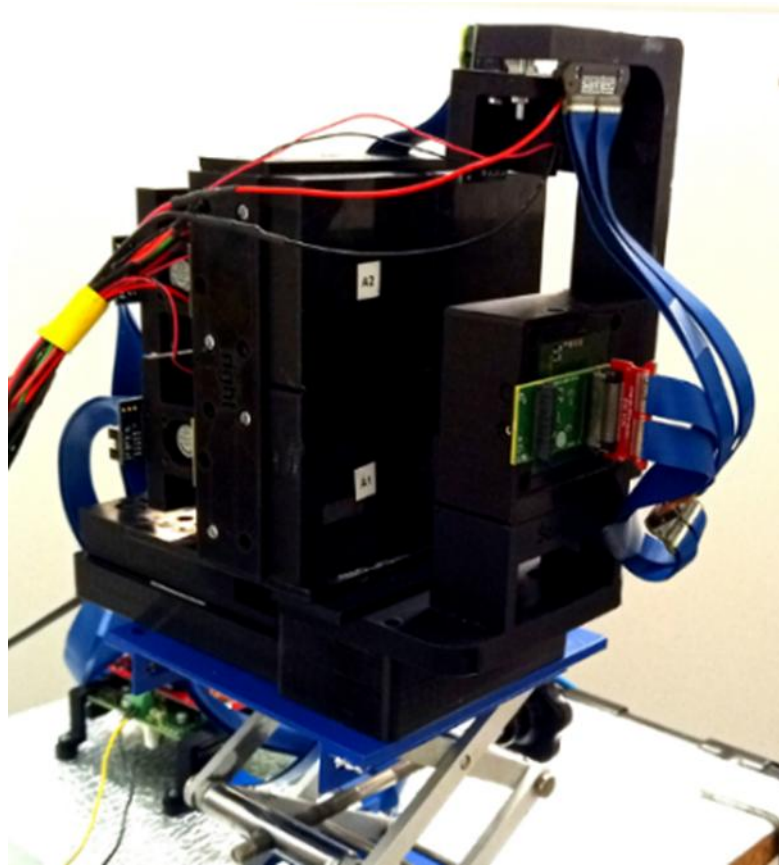


Figure 1 Photography of one i-TED Compton imager based on two detection planes and consisting of 5 position sensitive detectors based on  $\text{LaCl}_3(\text{Ce})$  crystals.

## 3 Exploring the high count-rate capability at CERN n\_TOF EAR2 for TOF experiments

Regarding the development and adaptation of i-TED for TOF experiments at high count rate several exploratory measurements have been carried out at CERN n\_TOF EAR2. The main aim of these

measurements was to investigate the count-rate limitations of i-TED, its intrinsic neutron-sensitivity and to develop techniques to optimize them.

Figure 2 shows several pictures of the experimental configurations utilized for these measurements.



Figure 2 (Left) i-TED detector placed at 90° with respect to the neutron beam at 36cm from the sample center. (Center) i-TED detector at an angle of about 125°. (Right) i-TED detector supplemented with 6Li-enriched polyethylene neutron absorber.

In order to test the count-rate capability of the detection system, a  $^{197}\text{Au}$  cylindrical sample of  $0.1 \times 20\text{mm}^2$  was measured at EAR2. Fig. 3 (left) shows the result of these measurements for two different energy-thresholds of about 100keV and 400 keV. In the resonances with largest instantaneous gamma-ray emission, like the one at 4.9 eV, one can appreciate severe dead-time effects. This effect is somewhat mitigated by increasing the electronic threshold in the i-TED detectors (red spectrum).

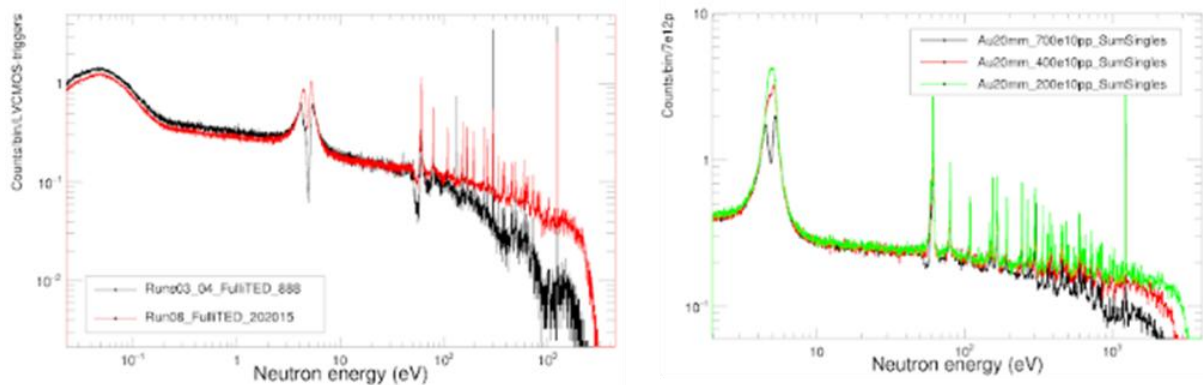


Figure 3 Results obtained for the  $^{197}\text{Au}(n,g)$  measurement at EAR2 with an i-TED module, using two different electronic thresholds (left) and for three different proton-beam intensities of 2E12, 4E12 and 7E12 protons/pulse.

However, the enhancement in detection threshold is not a suitable solution, particularly for the measurement of actinide-samples that are characterized with a rather soft gamma-ray spectrum. Additionally, several measurements were carried out at different proton-beam intensities (Figure 3-right). It can be concluded that, with the present state-of-the-art instrumentation, maximum count-rates of 0.5 Counts per micro-second can be accepted. However, for high gamma-yield samples or samples with a high intrinsic activity, this implies measuring at distances as far as 36 cm from the capture sample. It was found that this very-large distance detector-to-sample represents in turn a disadvantage in terms of intrinsic signal-to-background ratio because the efficiency attained for true capture gamma-rays coming from the sample is relatively small, when compared to the overall efficiency for background events from the surroundings. The situation did not improve noticeably

when the detector was placed upstream at an angle of about 125° (Figure 2-middle). Presently, this represents the main technical limitation for the implementation of the i-TED concept at EAR2 for the measurement of actinide samples. Under these circumstances, additional measurements were carried out in the laboratory in order to better understand the origin of the dead-time in the detection system. These measurements are reported below.

#### 4 Dead-time characterization in the laboratory

In order to investigate the detector response as a function of the count rate a series of measurements were carried out in the laboratory using a dedicated set-up. The latter consisted of an encapsulated <sup>22</sup>Na source with an activity of 2 MBq. The source was attached to a positioning drive and systematically moved to different distances from the front detector face in order to induce different count rates in the detector. The picture in Figure 4 the characterization set-up using one of the i-TED detectors.

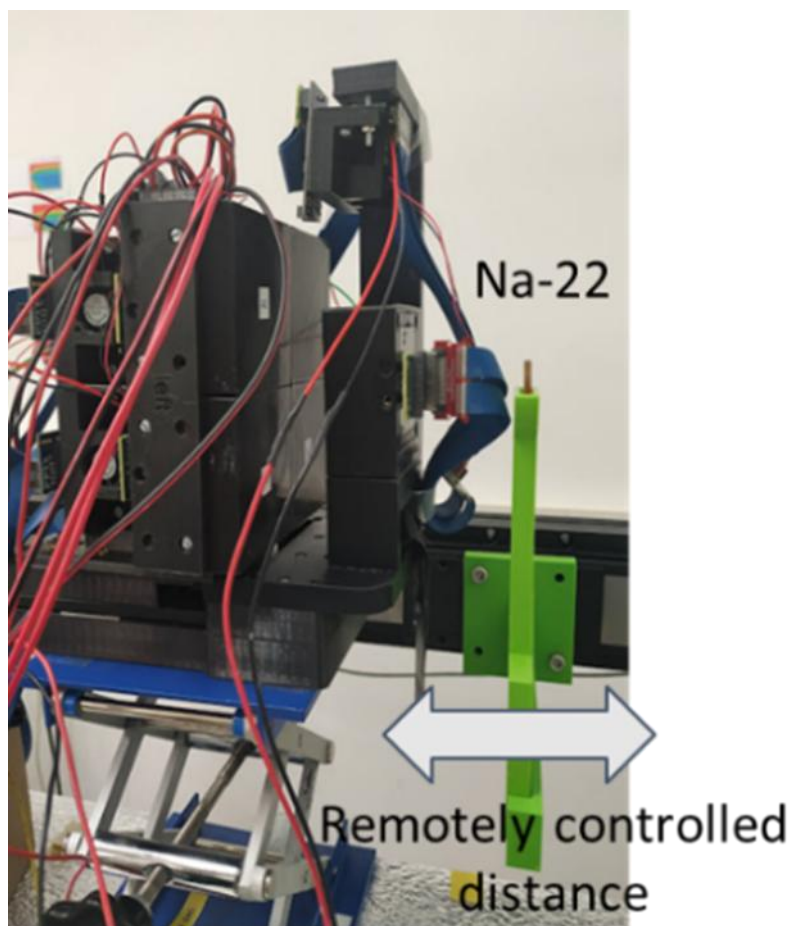


Figure 4 Picture of the set-up used in the laboratory to characterize the maximum count-rate capability and dead-time of the i-TED detection system.

A series of pulse-height spectra were taken for different source-to-detector distances. These spectra are shown in Figure 5.

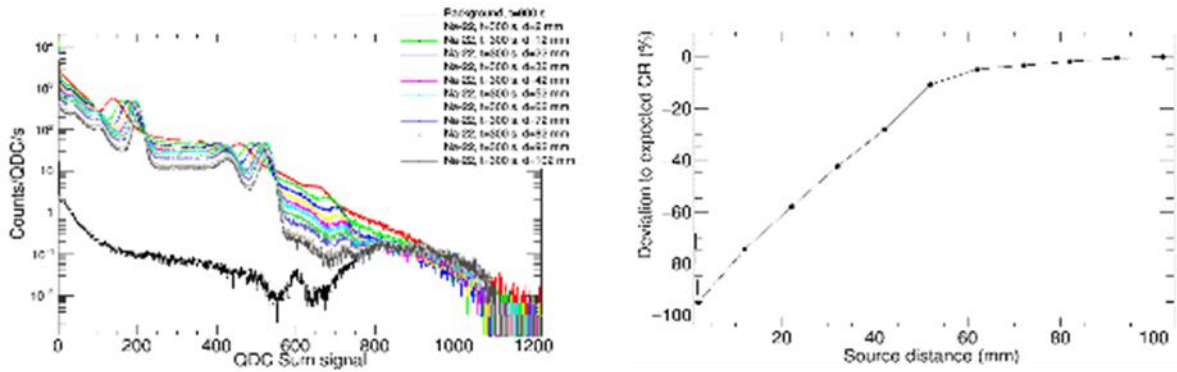


Figure 5 (Left) Pulse-height spectra obtained for different count rates varying the distance source-to-detector. (Right) Deviation with respect to expected count rate as a function of the gamma-ray source.

From these series of measurements, it was concluded that at distances of about 5 cm the absolute count rate starts to deviate with respect to the expected value (considering the subtended solid angle) due to dead-time effects. This count-rate corresponds to values of about 500 kHz per channel or per detector. This limitation is ascribed to the intrinsic performance of the TOFPET2 ASIC readout chip, which requires a certain time to process every single event [2].

In order to get further insight about the effect of the dead time in the event-reconstruction the correlation in pixel-multiplicity between scatterer (M1) and absorber (M2) detectors was studied for a time-correlation window of 100ns in one of the highest count-rate situations.

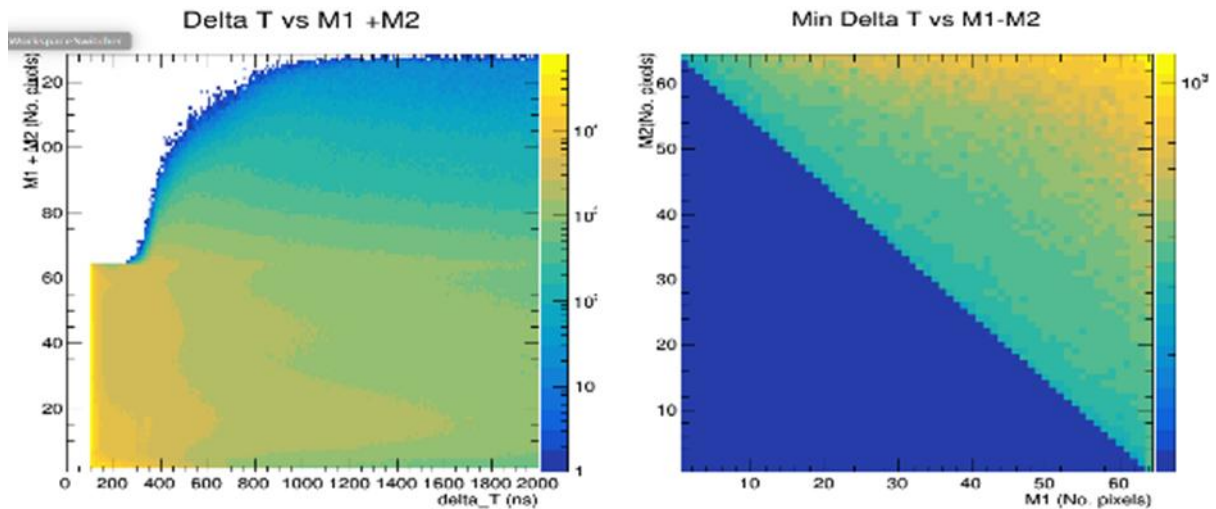


Figure 6 (Left) Total number of fired pixels in both detection planes (S and A) as a function of the time-difference Delta\_T between them in a high count-rate situation. (Right) Multiplicity correlation between two coincident events in the S detector (M1) and one A detector (M2) with minimum time separation shown in colour scale.

According to the results displayed in Figure 6, after the 100 ns coincidence window, the system still requires another 220 ns to recover. This effect reflects the total QDC integration time of each ASIC, which was equal to 320 ns. On the other hand, a full recovery is achieved for time intervals of less than 1  $\mu$ s.

This behaviour was also studied at the pixel-level, thereby looking at time-differences between two consecutive events in the same pixel. Results are shown in Figure 7, which demonstrates that the

minimum dead-time per pixel corresponds to the integration time window, which is of 320 ns and 80 ns for operating the ASIC in QDC- and TOT-modes, respectively.

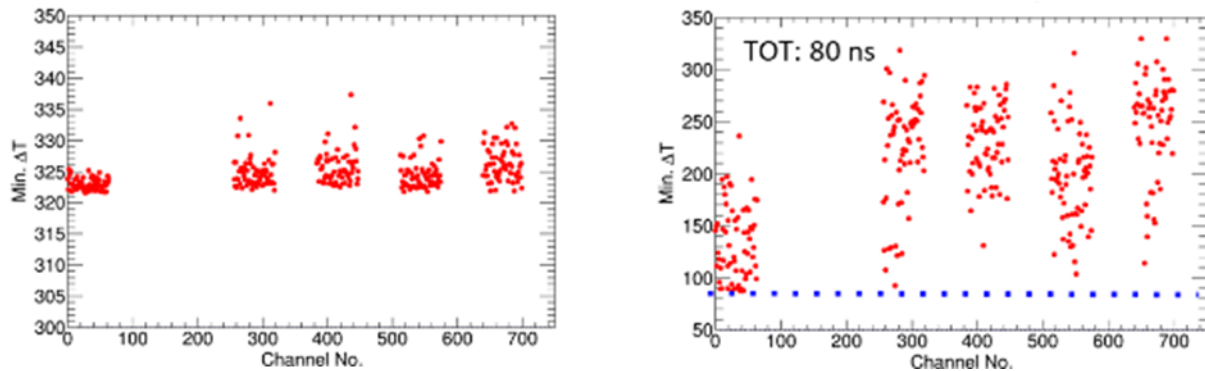


Figure 7 Minimum time interval for two consecutive events in QDC mode (left) and in TOT mode (right). Each group of events corresponds to the 64 pixels in each detector, being the first 64 pixels for the S-detector and the remaining 4 groups (of 64 pixels each) for the four detectors in the absorber plane.

The conclusion from this study is that the dead-time, and hence high count-rate capability, of the system could be reduced from 320 ns down to 80 ns, i.e. a factor of 4 by utilizing the readout ASICs in TOT mode. However, this configuration implies a significant deterioration of the energy resolution, which in turn limits the imaging capability of the system and hinders the application of Compton imaging for background rejection.

## 5 Development of techniques to mitigate the impact of dead-time effects

A methodology based on Machine-Learning (ML) was developed and applied in order to mitigate the impact of pixel dead-time in position- and energy-reconstruction. The implemented ML approach is based on autoencoders. The working principle of the autoencoder is schematically shown in Figure 8.

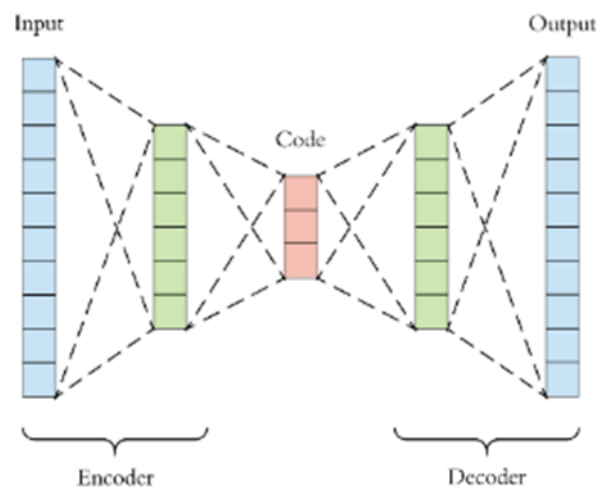


Figure 8 Schematic representation of the ML-algorithm based on encoders.

The encoder translates the dead-time affected input into a latent space (code) and the decoder provides a (corrected) output from the latent space. Ideally, the latent space is the minimum phase space required to describe the input and deliver an output. A fitting procedure is implemented to obtain a satisfactory output from the latent space.

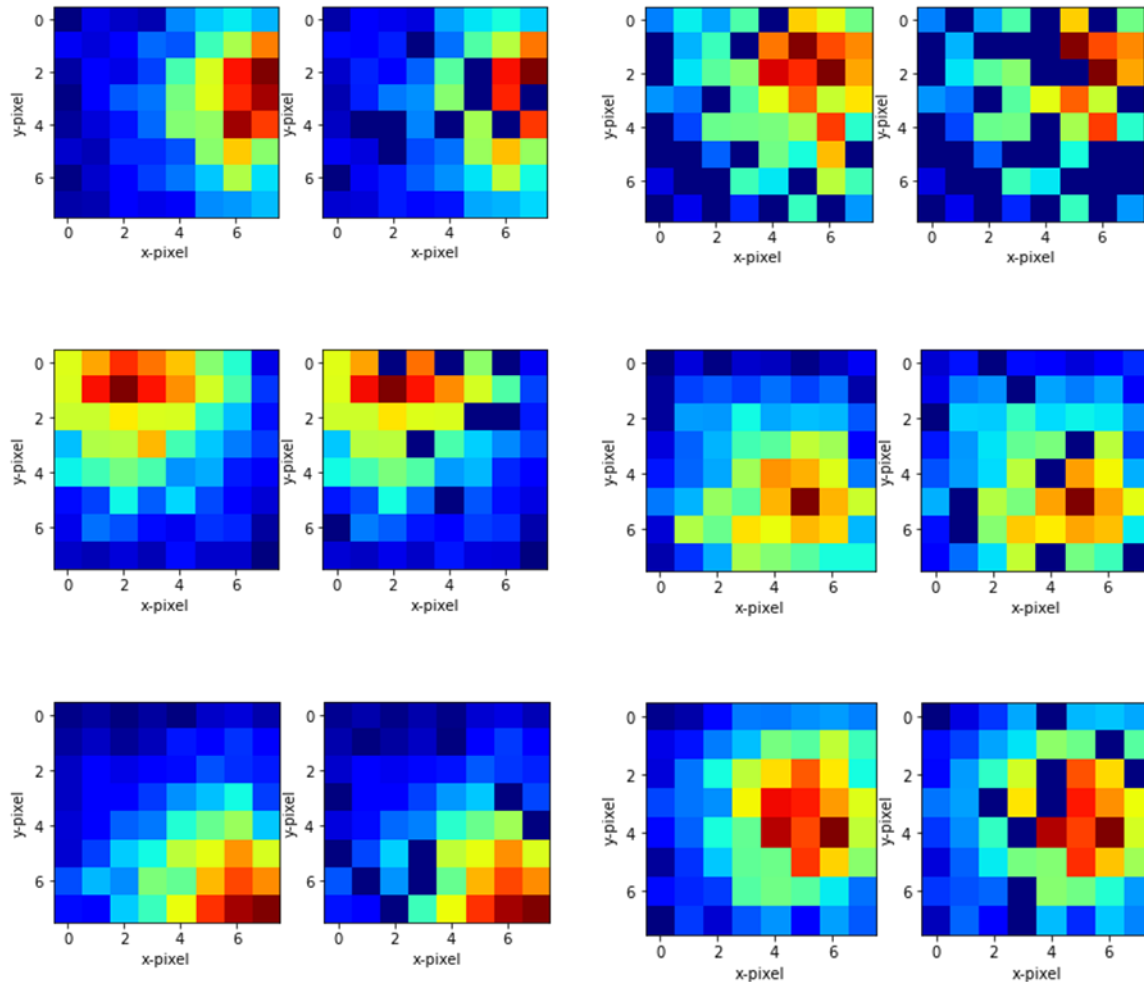


Figure 9 Several examples of pixel maps with pixels affected by dead-time effects (right distribution in each case) and the corresponding corrected distribution (left).

Figure 9 shows six different examples of pixel-map distributions corrected by means of the implemented autoencoder approach. In each case, the left distribution shows the processed pixel-map distribution, from the initially dead-time affected input data (right). When the number of affected pixels is small, the result is rather reliable. On the other hand, for distributions with a large number of pixels missing, the reconstructed distribution is less satisfactory. The performance of the algorithm can be quantified by inspecting the root-mean square-distribution per pixel between the input- and output-pixel maps (Figure 10).

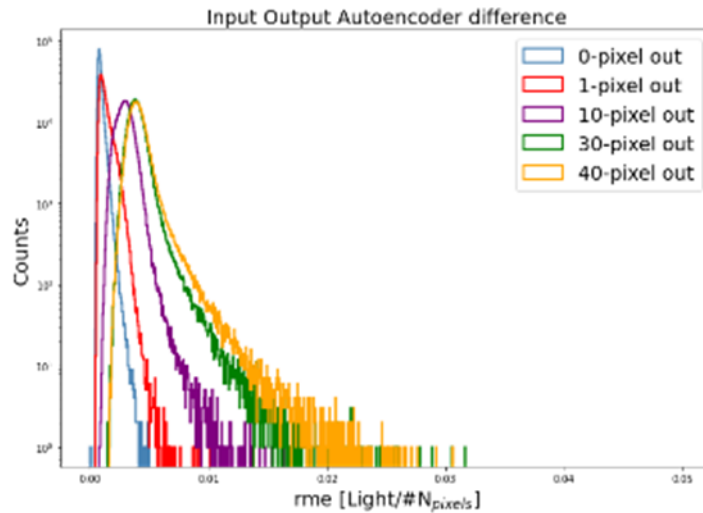


Figure 10 Root-mean square-distribution per pixel between the input- and output-pixel maps.

As it can be seen, for situations where a few pixels are missing the results are satisfactory. On the other hand, when 10 or more pixels are affected, the reconstructed distributions start to deviate significantly from the ideal case.

## 6 Implementation of neutron-background suppression techniques

Additionally, a technique was developed and implemented in order to minimize the intrinsic neutron-sensitivity of i-TED. To this aim, several Monte Carlo simulations were carried out with the Geant4 code (Figure 11-right) and, experimentally, the effect of a 6Li-enriched polyethylene (6LiPE) moderator with a thickness of 20 mm was explored at EAR2 using a graphite sample. The results are shown in Figure 11.

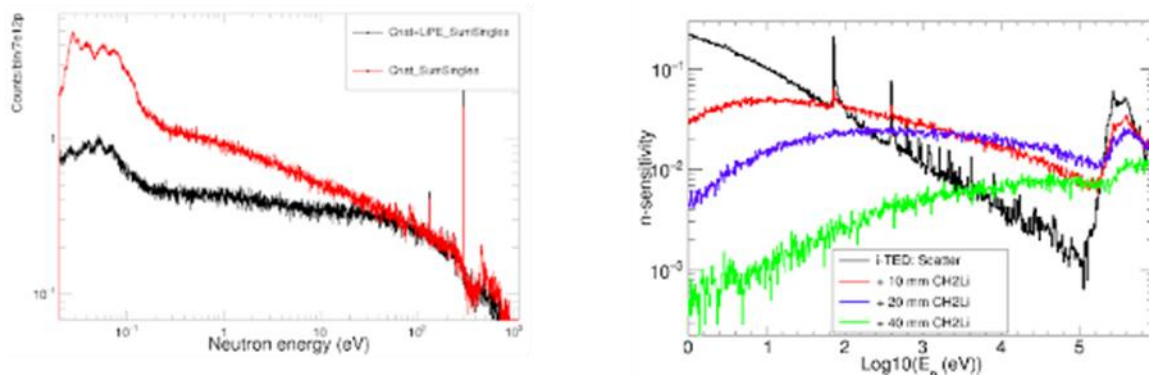


Figure 11 (Left) measurement of a graphite ( $^{nat}\text{C}$ ) sample to determine the intrinsic neutron-sensitivity of i-TED without any neutron moderator (red-line) and with a 20mm thick 6LiPE moderator (black-line). (Right) MC-simulation with Geant4 of the expected i-TED.

The experimental results obtained for the neutron-suppression are in good agreement with the MC-simulations, and show the effectiveness of the employed technique for reducing the intrinsic neutron sensitivity by up to a factor 4 in the low neutron-energy region. Beyond neutron-energies of 100 eV the effect of the neutron moderator is marginal, as it was expected from the MC simulations.

## 7 Summary and conclusions

Measurements and analysis have been carried out with an i-TED module at n\_TOF EAR2 in order to characterize its response to very high-count rates and to explore weaknesses and possible technical solutions.

The major technical limitation, of the actual i-TED system, is ascribed to the maximum count-rate capability of 500 kHz/detector, which is mainly constrained by the large number of readout channels (320 channels per module) and the ASIC-based readout front-end electronics required for such a large number of channels.

Possible solutions to the aforementioned limitation will depend on the availability of new-generation ASIC electronics capable of coping with higher count-rates.

So far, the alternative option is to perform experiments at EAR1 with i-TED, where it has shown an excellent capability for enhancing detection sensitivity in neutron-capture measurements [3].

## 8 References

- [1] C. Domingo-Pardo, i-TED: A novel concept for high-sensitivity (n,g) cross section measurements, Nuclear Inst. and Methods in Physics Research, A, Volume 825, p. 78-86 (2016)
- [2] <https://www.petsyselectronics.com/web/>
- [3] V. Babiano et al., Gamma-Ray position reconstruction in large monolithic LaCl<sub>3</sub>(Ce) crystals with SiPM readout, Nuclear Instruments and Methods in Physics Research A 931 (2019) 1-22
- [4] J. Balibrea-Correa et al., Machine-Learning aided 3D-position reconstruction in large LaCl<sub>3</sub> crystals, Nucl. Instr. And Methods A (2022)
- [5] V. Babiano-Suarez et al., First i-TED demonstrator: A Compton imager with Dynamic Electronic Collimation, Nucl. Instr. Meth. A (2021)
- [6] V. Babiano-Suarez et al., Imaging neutron capture cross sections: i-TED proof-of-concept and future prospects based on Machine-Learning techniques, The European Physical Journal A, Volume 57, Issue 6, article id.197 (2021).